sustainability

MDPI

Article

The Interconnection between Climate Cycles and Geohazards in Urban Areas of the Tourist Island of Mallorca, Spain

Juan A. Luque-Espinar [1,*], Rosa M. Mateos [1], Roberto Sarro [2], Cristina Reyes-Carmona [3] and Mónica Martínez-Corbella [2]

[1] Geological and Mining Institute of Spain from the National Research Council (IGME_CSIC), Urb Alcázar del Genil, edf. Zulema 4 bajo, 18006 Granada, Spain
[2] Geological and Mining Institute of Spain from the National Research Council (IGME_CSIC), Ríos Rosas 23, 28003 Madrid, Spain
[3] Department of Earth and Environmental Sciences, University of Milano-Bicocca, Piazza della Scienza 4, 20126 Milan, Italy
* Correspondence: ja.luque@csic.es

Abstract: The island of Mallorca has experienced major interventions and transformations of the territory, with unprecedented urban development related to growing tourism activity. In this paper, we present a spatio-temporal analysis—by using spectral analysis techniques—of climate cycles on the island of Mallorca (Spain) and their correlation with the occurrences of landslides and flash floods. Both geohazards are closely related to wet periods, which are controlled by different, well-known natural cycles: ENSO, the NAO, sunspot, etc. Geostatistical methods are used to map the distribution of rainfall, as well as a spatial representation of the spectral confidence of the different natural cycles, to define the hazardous areas on the island. The cycles with the greatest influence on rainfall in Mallorca are El Niño–Southern Oscillation (ENSO) (5.6 y and 3.5 y), the North Atlantic Oscillation (NAO) (7.5 y), and Quasi-Biennial Oscillation (QBO). Recorded events of both rockfalls and flash floods exhibit a strong correlation with the climate indices of QBO, ENSO, the NAO, and sunspot activity. This correlation is particularly pronounced with QBO, as this cycle has a higher frequency than the others, and QBO is observed as part of the other cycles in the form of increases and decreases during periods of higher ENSO, NAO, and sunspot values. However, the impact of flash floods is also significant in the southeast part of the island, despite its lower levels of rainfall. The most dangerous episodes are related to ENSO (6.4 y) and the NAO. The validation of the methodology employed is strengthened by incorporating information from the flash flood data, as it offers comprehensive coverage of the entire island, compared to the landslide database, which is confined to the Serra de Tramuntana region. The study reveals that the city of Palma and the municipality of Calvià, as well as the central and eastern urban areas of the island, are the most vulnerable regions to intense rainfall and its consequences.

Keywords: climate cycles; spectral analysis; geostatistic analysis; geohazards impact; urban areas

check for updates

Citation: Luque-Espinar, J.A.; Mateos, R.M.; Sarro, R.; Reyes-Carmona, C.; Martínez-Corbella, M. The Interconnection between Climate Cycles and Geohazards in Urban Areas of the Tourist Island of Mallorca, Spain. *Sustainability* **2024**, *16*, 4917. https://doi.org/10.3390/su16124917

Academic Editor: Hariklia D. Skilodimou

Received: 15 April 2024
Revised: 29 May 2024
Accepted: 31 May 2024
Published: 7 June 2024

Copyright: © 2024 by the authors. Licensee MDPI, Basel, Switzerland. This article is an open access article distributed under the terms and conditions of the Creative Commons Attribution (CC BY) license (https://creativecommons.org/licenses/by/4.0/).

1. Introduction

The Mediterranean region has experienced major transformations of the territory, with unprecedented urban development, mainly related to growing tourism activity. This is the case on the island of Mallorca (Spain); with a population of 1,200,000 people (census 2023), Mallorca represents one of the largest tourist destinations in the world. In the year 2023, Mallorca broke the record for tourist arrivals, with 14.4 million visitors, mainly concentrated in the coastal strip (a coastline of 850 km). The coastline of Mallorca is highly urbanized and has been severely modified by tourist activity, which represents 45.5% of the region's GDP [1].

Extreme weather events have severe impacts on Mediterranean coastal areas, often leading to cascading processes such as flash floods, coastal erosion, beach retreat, rockfalls,

and landslides in cliff areas [2]. Due to the high concentration of people and assets in exposed locations, the coastal fringe of Mallorca is particularly vulnerable to geohazards, which can result in severe and tragic impacts. A significant example of this occurred in Mallorca in October 2018 when an extraordinary convective rainfall event (400 mm in 6 h) triggered a devastating flash flood in the urban center of Sant Llorenç des Cardassar, resulting in 13 fatalities and severe damages [3].

In this context, effective land management, urban planning, and the adoption of preventive measures to minimize the impact of geohazards necessitate a deeper understanding of the natural processes that trigger extreme rainfall events [4]. The present study analyzes the influence of natural climatic cycles on the occurrence of rainy periods on the island of Mallorca and validates the results with available inventories of landslides in the Tramuntana range (NW of Mallorca) and flash floods across the entire island.

Rainfall-related geohazards are characterized by cyclical components [5,6]. Different authors have linked climate cycles, such as ENSO or the NAO, to major natural disasters in different parts of the world, including the Mediterranean area [6–9]. However, the specific behavior of these cycles has not yet been analyzed.

Among the different climatic cycles that have visible effects at a human scale, the following should be highlighted:

- Quasi-Biennial Oscillation (QBO): 2 and 2.9 years [10].
- El Niño–Southern Oscillation (ENSO) shows cycles of between 5 and 6 years [11], although it may be a harmonic component of the 11-year sunspot cycle. On the other hand, the warm phase of ENSO may range between 2 and 7 years [12].
- The North Atlantic Oscillation (NAO) shows cycles of between 6 and 10 years [13,14].
- The sunspot cycle [11] shows cycles of between 10.5 and 12 years.
- The Hale cycle [15] has associated cycles of between 20 and 25 years.
- There are other cycles associated with solar activity and lunar tidal cycles, such as 18.6, 26.8, and 47.6 years [16–18].
- Atlantic Multidecadal Oscillation [19,20].

Although many of these cycles are extensively discussed in the literature, QBO receives comparatively less attention regarding its correlation with other climatic cycles. Several authors have explored this relationship [21–24]. In some instances, it is only referenced in terms of its periodicity as part of broader cycles [25,26]. These climatic cycles show varying degrees of presence across different proxies in the Mediterranean region.

To uncover patterns and cycles in time series data, including climate data, spectral analysis is a powerful statistical technique that analyzes the distribution of power over different frequencies. It is widely used to identify patterns in long-term data series [17,27]. Spectral analysis is a powerful statistical technique for analyzing the distribution (over frequency) of the power contained in a signal and is widely used to identify patterns in long-term data series. The presence and spectral confidence of natural climate cycles in long-term series from rainfall stations [28,29] have been determined using spectral analysis. The Blackman–Tukey method is the most effective way to calculate the power spectrum, as it yields superior results when identifying climate cycles, and it provides a higher level of spectral confidence [5,17]. Each climatic cycle estimated through this method will provide a percentage value of statistical confidence.

Recognizing these patterns is crucial for managing geohazards, as there is a strong correlation between significant landslide or flash flood occurrences and periods of extreme rainfall. In the last hundred years, several extreme climatic events have been identified as producing widespread landslide activity in Spain [30]. Thus, the definition of the rainfall conditions that when reached or exceeded are likely to trigger failure is very relevant to forecasting rainfall-induced landslides. There are a lot of studies about the relationship between rainfall and landslide occurrence, which attempt to determine the rainfall-triggering thresholds [31–40]. However, few studies have investigated the impact of climatic cycles on the occurrence of landslides. Likewise, mountainous areas of Spain are particularly vulnerable to flash floods. It is noteworthy that many small to medium-sized

river basins in the western Mediterranean region, due to their highly urbanized, steep, and coastal locations, are particularly prone to short hydrological responses. These conditions can lead to large, sudden, and unexpected flows which can intensify flood damage. Thus, the eastern coastal region of the island of Mallorca has been identified as a high-risk area for flash floods.

Only a few studies have analyzed the link between climatic cycles and landslide occurrence [8,41,42]. In [42], the triggering factors for landslides in two very different geographical sectors, Ecuador and the South of Spain, are analyzed. In the case of the Loja Basin, the ENSO cycle shows a moderate positive correlation with accumulated rainfall in the wettest period, while for the South of the province of Granada, a positive correlation was found between the NAO and the WeMO (Western Mediterranean Oscillation) climate time series and the accumulated rainfall.

The bibliography on the relationship between climatic cycles and floods is more abundant, even when considering only studies within Europe. Thus, ref. [43] found that the relationship between ENSO and the occurrence and intensity of extreme rainfall in Europe is much less substantial than these phemoneas' relationship with the NAO or EA but is still significant in some regions. They demonstrate that flooding has strong links with climate variability, especially in southern and eastern Europe.

Moreover, ref. [44] shows that the influence of ENSO events is widespread, covering about 38% of the global land surface (excluding Antarctica). Southern and western North America, northern South America, and eastern Russia are influenced by the PDO. The NAO influences not only dry/wet conditions in Europe but also dry/wet conditions in northern Africa. Similarly, climate variability in southern Europe and northern Africa may be due to the concurrence of ENSO and the NAO.

In [45], different mechanisms for modulating the links between streamflow and the NAO are combined with topographical characteristics to explain the divergent influence of the NAO/western zonal circulation on the streamflow in different parts of central Europe. The study shows that a precipitation mechanism plays an important role in regulating winter flows in northwest Germany. This precipitation mechanism is also likely in southern central Europe, where correlations between the NAO and temperature are low. Finally, in the rest of the study area (northern central Europe, Alpine region), a precipitation–snow mechanism influences floods not only in winter but also in the spring/snowmelt period.

In Mallorca, the island suffered persistent and high precipitation in the period spanning from 2008 to 2010 that caused a large number of slope failures [46]. Ref. [5] carried out a temporal analysis, by means of spectral techniques, using a set of monthly hydrological and meteorological series on the Serra de Tramuntana mountain of Mallorca, where they showed the predominant influence of ENSO, the NAO, and sunspots in the rainiest periods. They also concluded that the cycle most directly related to the occurrence of landslides of greater magnitude is the NAO (7.5 y). However, this work focused exclusively on the temporal aspect and considered landslides but did not analyze the spatial distribution of the climatic cycles or examine the impact of other types of geological hazards.

Following on from [5], this study takes a broader approach to the influence, not only temporal but also spatial, of climatic cycles. To carry out this work, 62 meteorological stations distributed throughout the island were selected. Most of the rainfall stations have had at least daily rainfall data for the last 30 years. Based on these data, a spectral analysis was carried out, allowing us to identify the natural climate cycles of relevance in this Mediterranean region. The spectral confidence values of each climate cycle have been estimated using geostatistical methods to determine the degree to which the island of Mallorca has been affected. These values have been reclassified from 0 (not detected) to 4 (more than 99% spectral confidence). From the rainfall time series, other variables of interest have been estimated, such as the distribution of rainfall into dry-type years, average-type years and wet-type years. In addition, several years of the period under study have been selected according to the typology of the type of years, comparing the rainfall records.

To verify the results of our study, we spatially correlated the regions of Mallorca that are most prone to intense rainfall; an inventory of 423 landslides, most of them situated in road cuttings, catalogued in the Tramuntana range over the past three decades; and a database of floods comprising more than 300 records dating back to 1932.

2. The Island of Mallorca

The island of Mallorca is part of the Balearic archipelago in the western Mediterranean Sea. It has an area of 3677 km^2 and consists of various geomorphological domains, alternating ranges, and flat areas (Figure 1). The prominent Tramuntana range, in the northern part of the island, is an Alpine range with a maximum length of 90 km and an average width of 15 km. The line of peaks exceeds 600 m a.s.l, the central part being the highest, with numerous summits above 1000 m a.s.l., including Puig Major, the highest peak on the island (1445 m a.s.l.).

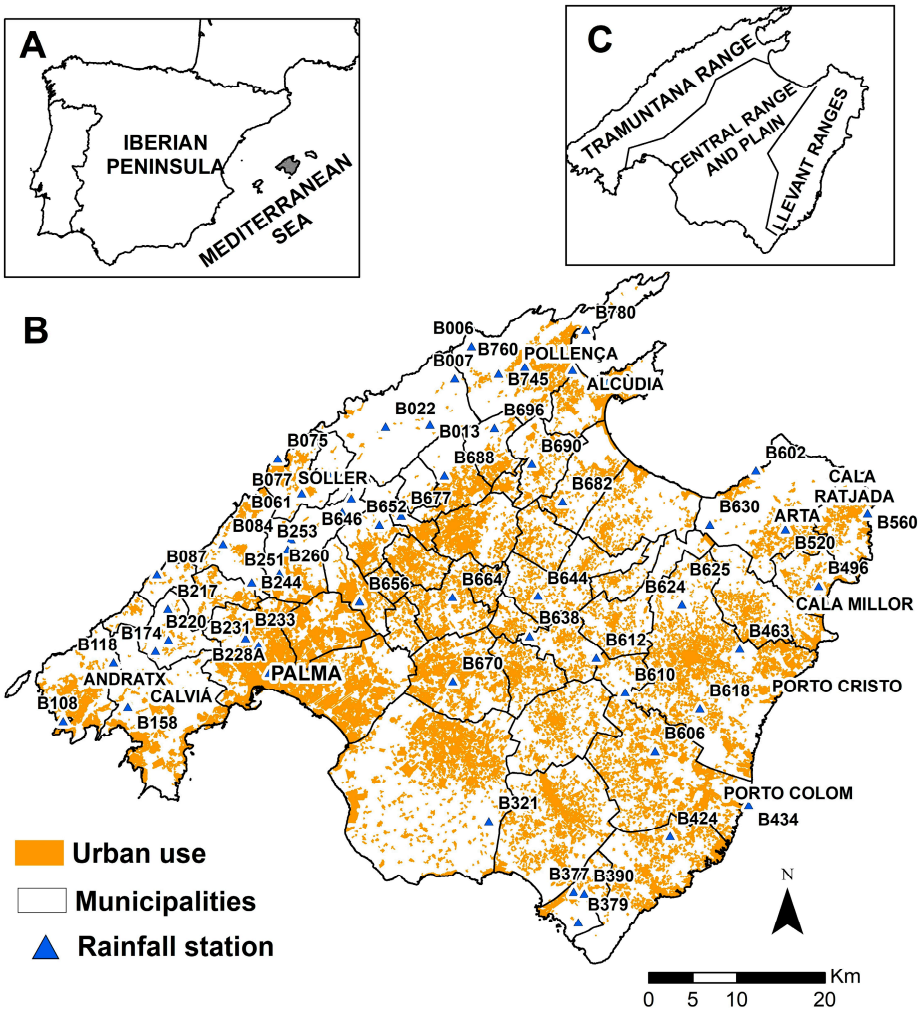


Figure 1. (**A**) Location of Mallorca in the western Mediterranean. (**B**) Rainfall stations used in the present work. (**C**) The main geomorphological domains on the island, highlighting the Tramuntana range in the northwestern part. The territory designated for urban use in Mallorca is indicated.

Mallorca has a typical Mediterranean climate, characterized by hot dry summers and mild winters, with its annual average temperature being 16.6 °C. The variability in precipitation in Mallorca shows values that range from 1400 mm (in the Tramuntana range) to around 300 mm at the southern end of the island. Rainfall is often in torrents, and it is concentrated into a very few days, with the maximum precipitation in 24 h exceeding 300 mm [47]. Between 2008 and 2010, Mallorca experienced the coldest and wettest winters

of the last 40 years. Its accumulated rainfall was twice the average, and values of intense rainfall up to 296 mm/24 h were recorded, very similarly to those calculated for a return period of 100 years. Additionally, high precipitation coincided with anomalously low temperatures, with abundant snowfall and freezing in the highest zones of the Tramuntana range. As a result, 66 landslides were recorded on the range, which seriously affected the road network and many facilities.

Figure 1 also displays the territory designated for urban use in Mallorca, which is notably extensive, comprising 25% of the island's total surface area. The Serra de Tramuntana, characterized by its rugged, step landscape and designation as a protected natural area, represents the portion of the island with the least urban development, starkly contrasting with other regions of Mallorca.

For the present work, we have updated the landslide inventory in the Tramuntana range [48]. Note that there are no data on landslides on the rest of the island. Flood data for the entire island were provided by the Balearic Islands Emergency Services. This documentation includes records of more than 300 instances of heavy rainfall, resulting in flooding between the years 1932 and 2010.

3. Methodology

The work methodology consists of the following steps (Figure 2):

1. Data Collection and Organization

The first step in this study is the collection and organization of relevant rainfall data. The data are organized by date, which is essential for performing spectral analysis. Additionally, information related to geohazards such as landslides and flash floods is also organized by date, triggering factors, and significant impacts.

2. Spectral Analysis

Once the data are organized, the next step is to perform spectral analysis on the rain data. Spectral analysis is used to identify patterns and cycles in the precipitation data.

3. Estimation of Spectral Confidence

The next step is to estimate the spectral confidence of the estimated cycles. Spectral confidence is a measure of how likely it is that a particular cycle is real and not just random noise. Thus, we can determine which cycles are most likely to be real and which are not.

4. Reclassification

The next step is to reclassify the spectral confidence values based on certain thresholds. This reclassification is carried out to simplify the analysis and make it easier to interpret the results. The reclassification is undertaken as follows: undetected cycle = 0; spectral confidence < 90% = 1; spectral confidence > 90% = 2; spectral confidence > 95% = 3; spectral confidence > 99% = 4.

5. Spatial geostatistical estimation

Once the spectral confidence values have been reclassified, the next step is to analyze and estimate them using geostatistical methods. By applying geostatistical methods, we can map the areas where the influence of the studied climatic cycles is most probable, thereby understanding the relationship between each point or sector and the climatic cycle.

6. Comparison with geohazard locations

The final step in this study is to compare the estimated climate cycles with the locations of landslides and flash floods on a georeferenced map. By comparing both, we can identify areas that are at a higher risk of landslides and flash floods.

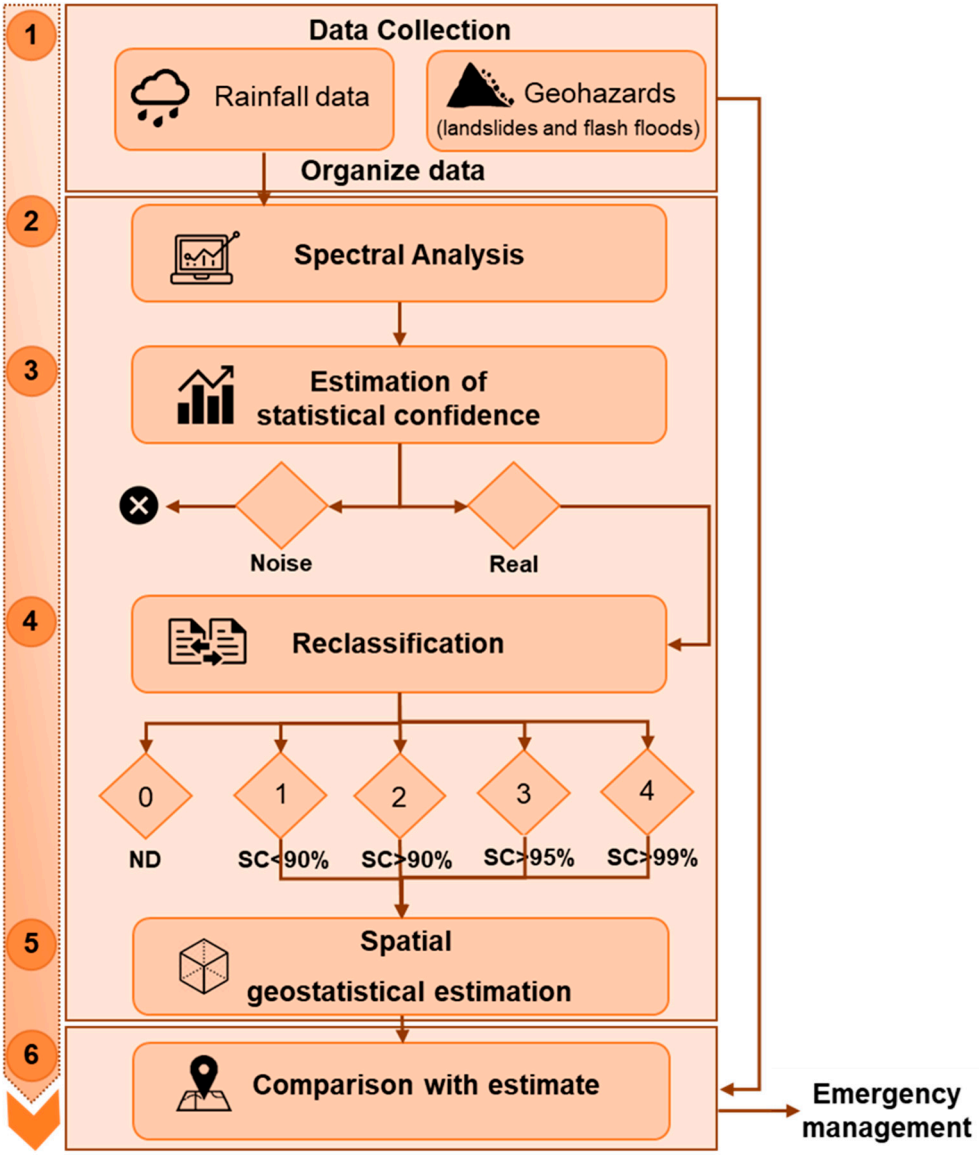


Figure 2. Workflow of the methodology.

Overall, this methodology is designed to provide a comprehensive analysis of the precipitation data and the geohazards associated with them. By organizing and analyzing the data in a systematic way, we can identify patterns and cycles in the precipitation data and estimate the spatial distribution of these cycles. This study aims to identify the correlation between precipitation patterns and the likelihood of hazards, specifically landslides and flash floods, and to understand the potential evolution of this correlation under various climate change scenarios.

3.1. Data Collection

3.1.1. Rainfall Data Series

We have exploited daily data series from AEMET (Spanish Meteorological Agency, Madrid, Spain) for 62 meteorological stations distributed across the island and mainly concentrated in the mountain ranges (Llevant, Central, and Tramuntana) (Figure 1). The stations have a minimum of 30 years of daily records, although a significant group exceeds 50 years. A total of 35 (56.5%) of the rain gauges are located in the Tramuntana range, which allows for an in-depth analysis of the rainfall data in the most hazardous region for landslides.

The maximum daily rainfall is concentrated in the Serra de Tramuntana, especially in the municipalities of Bunyola, Escorça, and Sóller. The annual rainfall data show very varied standard values, as do the daily records, although they essentially follow very similar spatial patterns and are conditioned by the topography of the island. From the meteorological series, the standard years of each meteorological series have been estimated in millimeters (Table 1). Dry-type years represent the mean values of the lower quartile of each rainfall series, average-type years represent the mean values of the entire rainfall record of each series, and wet-type years represent the mean values of the upper quartile of each rainfall series. In addition, analysis of the rainfall series studied has made it possible to identify a series of years for which the stations have rainfall values similar to the estimated years (Table 1). In this sense, the years 1983 and 1999 were very dry; the years 1985 and 2003 show values similar to those of the average; and finally, the years 1972 and 2008 were wet years.

Table 1. Estimated statistic values of the estimated years and selected natural hydrological years (in mm).

	Dry Year				**Average Year**				**Wet Year**		
Type	473	269	862	Type	662	382	1223	Type	1068	605	2008
YEAR	**MEAN**	**MIN**	**MAX**	**YEAR**	**MEAN**	**MIN**	**MAX**	**YEAR**	**MEAN**	**MIN**	**MAX**
1983	347	126	667	1985	670	357	1500	1972	994	536	1725
1999	373	167	756	2003	708	343	1333	2008	896	474	1885

3.1.2. Landslide Inventory

Information on landslides is only available in the Serra de Tramuntana [49]. Over the past 30 years, 423 landslides occurred in the Tramuntana range, with 91% of these being rockfalls and the remaining 9% being earth landslides, complex landslides, and debris flows. The landslide inventory from the last 30 years is more comprehensive, including information on the magnitude of the events, their precise location, and the date of their occurrence. Figure 3 shows the temporal distribution of the landslide events, with the year 2016 standing out, with 60 landslides. Most of these records were provided by the Road Maintenance Service of Mallorca and are related to small rockfalls (<100 m^3) with the source areas located in road cuttings. If we only consider the magnitude of the rockfalls in natural slopes, three of the largest ones took place during the rainy period 2008–2010 (Figure 2). Table 2 shows the main parameters of the five largest natural rockfalls inventoried and dated during the spanning period 1991–2020. The largest one took place on the night of 19 December 2008. The Son Cocó rock avalanche (Alaró)—with a length of 650 m—destroyed the pine wood in its path, leaving blocks over an area of 60,000 m^2 and 300,000 m^3 in volume (Figure 2). Some of the blocks had a volume of over 1500 m^3 and were several tons in weight.

In addition to the 5 major landslides previously mentioned, 17 more dated events have been added. All the events occurred within a few years, with the majority, 15 in total, concentrated during the rainy period of 2008–2010. In 2008, there was a peak in the QBO and ENSO cycles, whose influence extended into early 2009. The year 2010 showed a strong influence from QBO and sunspots. During 2008, 394,800 m^3 of rock was mobilized, with 66,500 m^3 in 2010.

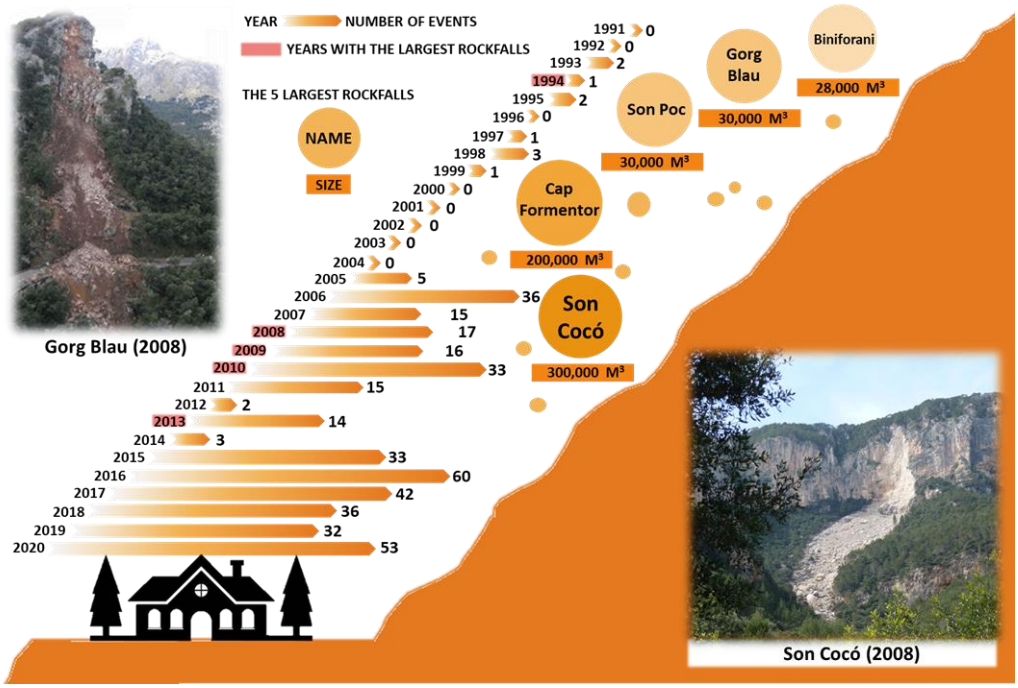


Figure 3. Distribution of the 423 landslide events registered during the past 30 years (1991–2020) in the Tramuntana range of Mallorca and the temporal location of the five largest rockfalls (>28,000 m^3). There are no records for the first 2 years. Photos of two of the largest rockfalls that took place during the rainy cold period 2008–2010. Right: The Son Cocó rock avalanche in December 2008, the largest rockfall (300,000 m^3). Left: The Gorg Blau rockfall (30,000 m^3), also in December 2008.

Table 2. Twenty two natural-slope rockfalls registered during the past 30 years in the Tramuntana range. Most of them occurred during the rainy cold period spanning from 2008 to 2010. LS: Land Slide.

Date	Municipio	Type	RS	Vol	QBO	ENSO	NAO	SSPOT	Damage
Sep-94	Pollenssa	Rock Fall	97.3	200,000			MAX		Ma_2210 road and 1 fatality
Oct-08	Soller	LS	64.0	1500	MAX	MAX			Powe station
Nov-08	Escorca	Rock Fall	128.5	16,000	MAX	MAX			Path
Dic-08	Escorca	LS	190.2	7000	MAX	MAX			Ma_10 road
Dic-08	Escorca	LS	61.7	12,000	MAX	MAX			Cala Tuent road
Dic-08	Esporles	LS	178.3	200	MAX	MAX			Es Verges road
Dic-08	Alaro	Rock Fall	150.2	300,000	MAX	MAX			Land, pine wood
Dic-08	Escorca	Rock Fall	35.1	30,000	MAX	MAX			Ma_10 road
Ene-09	Bunyola	Rock Fall	33.8	28,000					Land
Ene-09	Calvia	LS	26.5	100					Building
Ene-10	Andratx	Rock Fall	93.1	10,000	≈MAX			≈MAX	Ma_10 road
Feb-10	Esporles	Rock Fall	28.6	14,000	≈MAX			≈MAX	Barn
Mar-10	Andratx	LS	44.5	30,000	≈MAX			≈MAX	Ma_10 road
Abr-10	Estellencs	LS	20.2	3000	≈MAX			≈MAX	Ma_10 road
May-10	Banyalbufar	LS	120.3	4500	≈MAX			≈MAX	Ma_10 road
Oct-10	Andratx	Rock Fall	69.2	5000	≈MAX			≈MAX	Ma_10 road
Nov-11	Andratx	Rock Fall	104.0	2000	MAX	MAX	MAX		
Sep-12	Fornalutx	Rock Fall	27.9	2500					Ma_10 road
Nov-12	Banyalbufar	Rock Fall	30.8	200					
Mar-13	Bunyola	Rock Fall	23.1	30,000	MAX	MAX	MAX		3 houses, Pine wood
May-13	Banyalbufar	Rock Fall	72.1	400	MAX	MAX	MAX		Road
Feb-15	Soller	Rock Fall	67.2	200			MAX		Road

3.1.3. Flash Flood Inventory

Between 1932 and 2010, the Balearic Islands Emergency Services recorded more than 300 episodes of heavy rainfall all over the island that resulted in flooding, causing varying degrees of damage, with some instances resulting in injuries and deaths (Table 3). Rainfall records represent the accumulation of precipitation over short temporal durations, generally not surpassing 48 h, yet the availability of such information may not always be ensured within the utilized database. These totals range from 8 mm to 400 mm, with a median of 128 mm and a mean of 143 mm. The first quartile is 78 mm, and the third quartile is 193 mm.

After 2010, the system for collecting information on floods was changed, and data on rainfall are no longer included. Instead, the focus is on the damage caused and the municipalities affected, as well as the month in which the floods occurred. This type of record begins in 2015 and continues until 2021 (Table 3), resulting in an information gap between 2010 and 2015. During this period, the number of municipalities affected by floods ranges from 24 (2015) to 74 (2017), but 2018 recorded the highest number of casualties, injuries (89), and fatalities (13). The parameters utilized include the annual mean of maximum recorded rainfall (Max rain), the date of the flash flood's occurrence (Date flow), rainfall recorded at the nearest climatic station, the relative value of the QBO index, the relative value of the ENSO index, the relative value of the NAO index, the relative value of the sunspot index, the maximum value of the index in the cycle (MAX), the close to maximum value (ALMOST (CLOSE) MAX), and the fast increasing value (FI) to MAX. These cycles have a significant impact on landslide occurrence.

Regarding Table 3, the following observations can be made. Between 1951 and 2018, 75 flood episodes were recorded. Considering the values of the maximum recorded rainfall, there is generally a coincidence of maximum spectral values from at least two cycles, especially when there is more than one flood episode per year (QBO and ENSO, QBO and the NAO). It is also deduced that individually, between 32% (sunspot) and 36% (QBO) of the floods have a direct relationship with a given climatic cycle. Additionally, 22% of the flood episodes have no direct relationship with the cycles mentioned in Table 3, and in all cases, these are single episodes. This behavior (or degree of influence) is spatially represented in the Section 4.3.

As previously mentioned, the information about floods is not very precise because there are no direct water flow measurements in the watershed where they occur, and there is not always a rain gauge station in the same watershed. In this regard, Table 3 summarizes the information related to these events. Based on Table 3, logistic regression was performed. The MAX values of the climatic cycles were transformed into 1 and the rest into 0.

Figure 4a shows the correlation matrix between all the variables in Table 3. The following observations are noteworthy. The correlation between max rainfall and the other variables shows the highest significance with QBO and ENSO and the lowest with RS. The RS variable shows a very similar correlation with all the cycles. Finally, the most significant relationship between cycles is QBO–sunspot.

These correlation results were expected given that precipitation, both from the perspective of the time series and the existing point values, has different degrees of influence from the climatic cycles affecting the island. Finally, Figure 4b represents the logistic regression model as an example. As seen in Figure 4a, the best correlation is between rainfall and the climatic cycles. This model indicates that as the precipitation value increases, so does its relationship with the QBO cycle.

Table 3. Correlation between rainfall causing flash floods and the relative values of key natural climatic cycle indices.

Year	Max Rain	Date	RS	QBO	ENSO-SOI	NAO	SSPOT	Year	Max Rain	Date	RS	QBO	ENSO-SOI	NAO	SSPOT
		Flash Flood								Flash Flood					
1951	1427							**1983**	667	Ago-83	328				
1952	965	Nov-52	91	MAX				**1984**	1038						
1953	889							**1985**	1500	Oct-85	168	MAX	MAX		
1954	1296							**1986**	1580	Sep-86	193		MAX	MAX	
1955	1300	Sep-55	96.3	MAX	MAX			**1986**	1580	Nov-86	140		MAX	MAX	
1956	880							**1987**	1448						
1957	1144	Oct-57	400	MAX			≈MAX	**1988**	914	Sep-88	194				
1958	955	Oct-58	349					**1989**	1075	Sep-89	410				
1959	1670	Oct-59	351	MAX		MAX	MAX	**1990**	1365	Ago-90	91.6	≈MAX		MAX	MAX
1959	1670	Sep-59	234	MAX		MAX	MAX	**1990**	1365	Oct-90	480	≈MAX		MAX	MAX
1960	1484							**1991**	1409	Ene-91	169			≈MAX	MAX
1961	669	Nov-61	129					**1991**	1409	May-91	110			≈MAX	MAX
1962	1310	Sep-62	341					**1991**	1409	Ago-91	175			≈MAX	MAX
1962	1310	Oct-62	90					**1992**	1027					MAX	
1963	1223	Sep-63	106					**1993**	723						
1964	1060	Oct-64	61		MAX	MAX		**1994**	959					MAX	
1965	802	Sep-65	44					**1995**	901				MAX		
1966	895	May-66	80	MAX				**1996**	2008	Sep-96	156		MAX		
1967	857	Sep-67	7.9					**1997**	1070						
1967	857	Dic-67	108					**1998**	1017	Nov-98	140			MAX	
1968	1081	Jun-68	43		MAX			**1999**	751						
1969	1391	Abr-69	81	MAX			MAX	**2000**	879						
1969	1391	Nov-69	44.1	MAX			MAX	**2001**	1615	Sep-01	150				MAX
1969	1391	Sep-69	25	MAX			MAX	**2001**	1615	Nov-01	226				MAX
1970	1100							**2002**	1838	Jul-02	57.5	MAX		MAX	MAX
1971	1708	Sep-71	363	MAX	MAX		MAX	**2003**	1333						
1971	1708	Oct-71	62	MAX	MAX		MAX	**2004**	1533	Dic-04	135	MAX		MAX	
1971	1708	Nov-71	98	MAX	MAX		MAX	**2005**	1149						
1972	1725	Ene-72	86			MAX		**2006**	1666	Dic-06	252	MAX		MAX	
1972	1725	Oct-72	91			MAX		**2007**	1295	Abr-07	273		FI		
1972	1725	Dic-72	223			MAX		**2007**	1295	Ago-07	97.5		FI		
1973	1670	Ene-73	119	MAX			MAX	**2007**	1295	Sep-07	42.2		FI		
1973	1670	Sep-73	270	MAX			MAX	**2007**	1295	Oct-07	241		FI		
1973	1610	Oct-73	131	MAX			MAX	**2007**	1295	Nov-07	49.5		FI		
1974	1694	Feb-74	454		≈MAX	MAX		**2008**	1885	Sep-08	107	MAX	MAX		
1974	1694	Mar-74	516		≈MAX	MAX		**2008**	1885	Oct-08	63	MAX	MAX		
1974	1694	Sep-74	17.1		≈MAX	MAX		**2008**	1885	Nov-08	50	MAX	MAX		
1974	1694	Oct-74	130		≈MAX	MAX		**2008**	1885	Dic-08	202	MAX	MAX		
1975	1538	Jun-75	37.9					**2009**	1601	Sep-09	347				
1975	1538	Ago-75	66					**2010**	1522	May-10	178		FI		FI
1975	1538	Dic-75	210					**2010**	1522	Sep-10	54		FI		FI
1976	1216	Ago-76	132					**2010**	1522	Oct-10	64		FI		FI
1976	1216	Nov-76	183					**2011**	1193			MAX	MAX	MAX	
1977	1444							**2012**	996						
1978	1740	Ene-78	282	MAX		MAX		**2013**	1553			MAX	MAX	MAX	MAX
1978	1740	Oct-78	215	MAX		MAX		**2014**	1136						≈MAX
1979	1468	Feb-79	162			≈MAX		**2015**	1083					MAX	
1979	1468	Sep-79	48			≈MAX		**2016**	1364			MAX			
1980	1463							**2017**	1174					MAX	
1981	883	Abr-81	279					**2018**	1536				MAX		
1982	1220	Nov-82	126			MAX	MAX								

(a)

	Year	Max rain	RS	QBO	ENSO	NAO	SSPOT
Year	1.00	0.13	− 0.16	− 0.05	0.29	0.07	0.01
Max rain	0.13	1.00	0.23	0.39	0.35	0.26	0.29
RS	− 0.16	0.23	1.00	0.15	0.04	0.18	0.16
QBO	− 0.05	0.39	0.15	1.00	0.10	0.07	0.41
ENSO	0.29	0.35	0.04	0.10	1.00	− 0.02	− 0.04
NAO	0.07	0.26	0.15	0.07	− 0.02	1.00	0.09
SSPOT	0.01	0.29	0.16	0.41	− 0.04	0.09	1.00

(b)

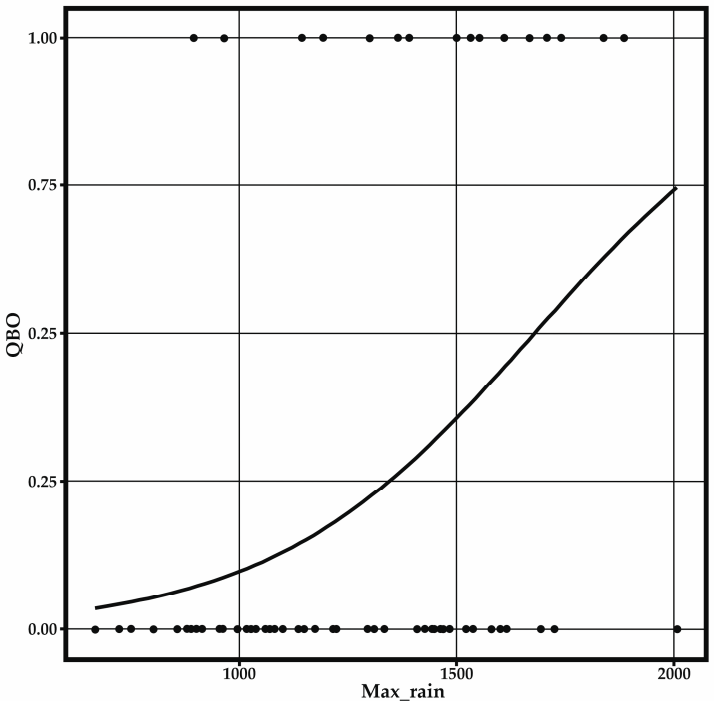


Figure 4. (**a**) Correlation matrix of the variables in Table 3. (**b**) Logistic regression model of max_rainfall and QBO.

3.2. Spectral Analysis

Spectral analysis or harmonic analysis [27,50,51] is a statistical technique used to identify cyclic components in a time series. The signal component represents the structured part of the time series, made up of a small number of embedded periodicities or cycles repeated over a long time. This information has a random component, or noise, which may be white noise but will more often be red noise. The time series are represented by a finite number of measurements at regular or irregular time intervals. The presence of trends in time series refers to the cyclic component of a longer period. These trends, plus real trends and other factors, give rise to low-frequency noise or red noise.

In this context, the time series is a linear combination of sinusoidal functions of known periods but of unknown amplitudes and phases. The modulus of the amplitude is linked to the variance in the time series and is related to the oscillation at each frequency. The representation of the square of the modulus versus frequency is known as the power spectrum. The indirect method proposed by [52] has been used due to it being a robust approach which yields good results in this kind of study [5].

The power spectrum [53] is calculated from the covariance function by Equation (1):

$$\hat{S}(\omega) = \frac{1}{\pi}\left\{\lambda(0)\hat{C}(0) + \sum_{k=1}^{M}\lambda(k)\hat{C}(k)\cos(\omega k)\right\} \quad (1)$$

where:

$\hat{S}(\omega)$: Estimated power spectrum for frequency ω,

$\hat{C}(k)$: Estimated covariance function for the k-th lag,

cos(·): Cosine,

$\lambda(k)$: Weighting function, known a lag window, which is used to give less weight to the covariance estimates as the lag increases.

For large lags, the estimated covariance function is less reliable. The lag window used was the Tukey window, following Equation (2):

$$\lambda(k) = \frac{1}{2}\left\{1 + \cos\left(\frac{\pi k}{M}\right)\right\} \quad (2)$$

M means the maximum number of lags for the covariance function used in the spectral estimation. $N - 1$ is the maximum number of lags, where N is the number of experimental data. However, with large values for M, a great number of peaks will be seen in the estimated power spectrum, with most representing spurious cycles. When M is very small, significant cycles will not be seen in the estimated power spectrum. For this reason, we used a value of M = N/2 in order [8,25,54,55] to resolve the peaks and a value of M = N/4 to determine which peaks are the most significant.

Confidence levels were estimated for the inferred power spectrum using a small value for N. The approach of this research consists of fitting a background power spectrum with no cyclic component but rather a smooth continuous spectrum, which is carried out by fitting the spectrum of an autoregressive process of order one. We then take into account the known result for the one-sided confidence band of the power spectrum estimator (Equation (3)):

$$P\left(v\frac{\hat{S}(\omega)}{S(\omega)} < \chi^2_{v,\alpha}\right) = 1 - \alpha \quad (3)$$

where

P(·): Probability operator

$\hat{S}(\omega)$: Power spectrum estimate for frequency ω.

S(ω): Underlying power spectrum for frequency ω.

v: Number of degrees of freedom. For the Blackman–Tukey estimate with a Tukey lag window, the number of degrees of freedom is 2.67 N/M.

$\chi^2_{v,\alpha}$ is the α quantile of a Chi-square distribution with v degrees of freedom.

α: Significance level.

For this study, we established five confidence levels (CLs): 0%, <90%, 90%, 95%, and 99%.

When the cycles are well identified, simulations can be performed to reproduce their behavior [5]. In this sense, calculating the amplitude and frequency for each cycle is necessary and is added to the most representative cycles.

In particular, the Lomb–Scargle periodogram [54,55] was employed as the technique for assessing the significance of the registered spectral peaks. To ensure the relevance of all the identified peaks, spanning both low and high frequencies, the Monte Carlo permutation test was utilized [17].

3.3. Geostatistical Estimation

Geostatistics [56–58] is widely accepted in science as a methodology for solving estimation problems based on the Theory of Regionalised Variables. These variables are distributed in space and show a correlation structure or spatial variability, represented by the variogram function, representing a structured and a random part [59]. The variogram is an intrinsic random function that represents half of the mean square increments of the spatial variable for distant points, vector h (Equation (4)).

$$\gamma(h) = 1/2E\{Z(x) - Z(x+h)\}2 \quad (4)$$

The variogram is therefore a vector function that quantifies the variance in the first-order quadratic increments of the function. The variogram allows the spatial variability in the variable to be analyzed as a function of distance, thus revealing the structure of the variation in the variable. The unbiased estimator of the variogram function is obtained from the data by means of Equation (5).

$$\gamma(h) = \frac{1}{2NP(h)} \sum_{i=1}^{NP(h)} \{z(x_i) - z(x_{i+h})\}^2 \quad (5)$$

where $z(x_i)$ and $z(x_{i+h})$ are the observed values of the variable at points x_i and x_{i+h}; $NP(h)$ is the number of distant data pairs h. Once the experimental variogram is computed, a theoretical model is fitted and incorporated into the spatial geostatistical estimation by kriging.

4. Results

4.1. Spectral Analysis

The rainfall in Mallorca shows an irregular spatial distribution, especially in the Tramuntana range. The topography of this range imposes the climatic variations typical of mountainous regions: higher elevations and heavy precipitation [47].

The highest values of spectral confidence estimated in the climate cycles correspond to 5.6 y (ENSO), 7.5 y (the NAO), 3.5 y (the ENSO), QBO, and 6.4 y (ENSO or NAO).

Figure 5 shows some representative daily rainfall records for the island of Mallorca and the results of the spectral analysis. The rainfall gauge analyzed shows a multitude of climatic cycles with different spectral confidence values, reflecting the complexity of Mallorca's climate. Figure 6 shows the main cycles estimated according to the number of detections and the highest spectral confidence values determined.

4.2. Spatial Estimation of the Influence of Climatic Cycles

The results of the spectral analysis have made it possible to identify the climatic cycles with the most influence on rainfall on the island of Mallorca. The spectral confidence values estimated at each rainfall station have been reclassified from 0 (not detected) to 4 (more than 99% spectral confidence) and have been estimated using geostatistical methods to determine the degree of influence of each climatic cycle (Figure 7). However, when there are a significant number of stations where the cycle has not been detected, a dichotomous transformation has been chosen, i.e., observed (1) or not observed (0), as in the case of ENSO (6.4 y) (Figure 7e), sunspots (11.2 y) (Figure 7f), and HALO (22.4 y) (Figure 7g). Furthermore, Figure 7 presents select examples of estimation errors (Figure 7a',b',e',g'). The distribution of the estimation errors remains consistent across all cases, with similar magnitudes of error observed. These errors, observed across both OK and IK methodologies, underscore the need to increase the station coverage in sectors exhibiting heightened estimation discrepancies.

It should be noted that the experimental variograms obtained show great continuity, reflecting a well-correlated variable in space. This continuity means that the fitted variograms exhibit a low nugget effect percentage, indicating that the unstructured part of the estimation has little influence. Moreover, the model variogram shows a high degree of overlap with the experimental variogram; therefore, the fit quality is very good. This has allowed a good fit in all cases to a spherical variogram model, with a nugget effect in all cases (less than 25% of sills) and well-defined sills. The southern part of the island, due to the smaller number of meteorological stations there, contributed small uncertainties to the estimation, which is why some estimated cycles show discontinuities in the mapping, as is the case with ENSO = 5.6 y and sunspots = 11.2 y.

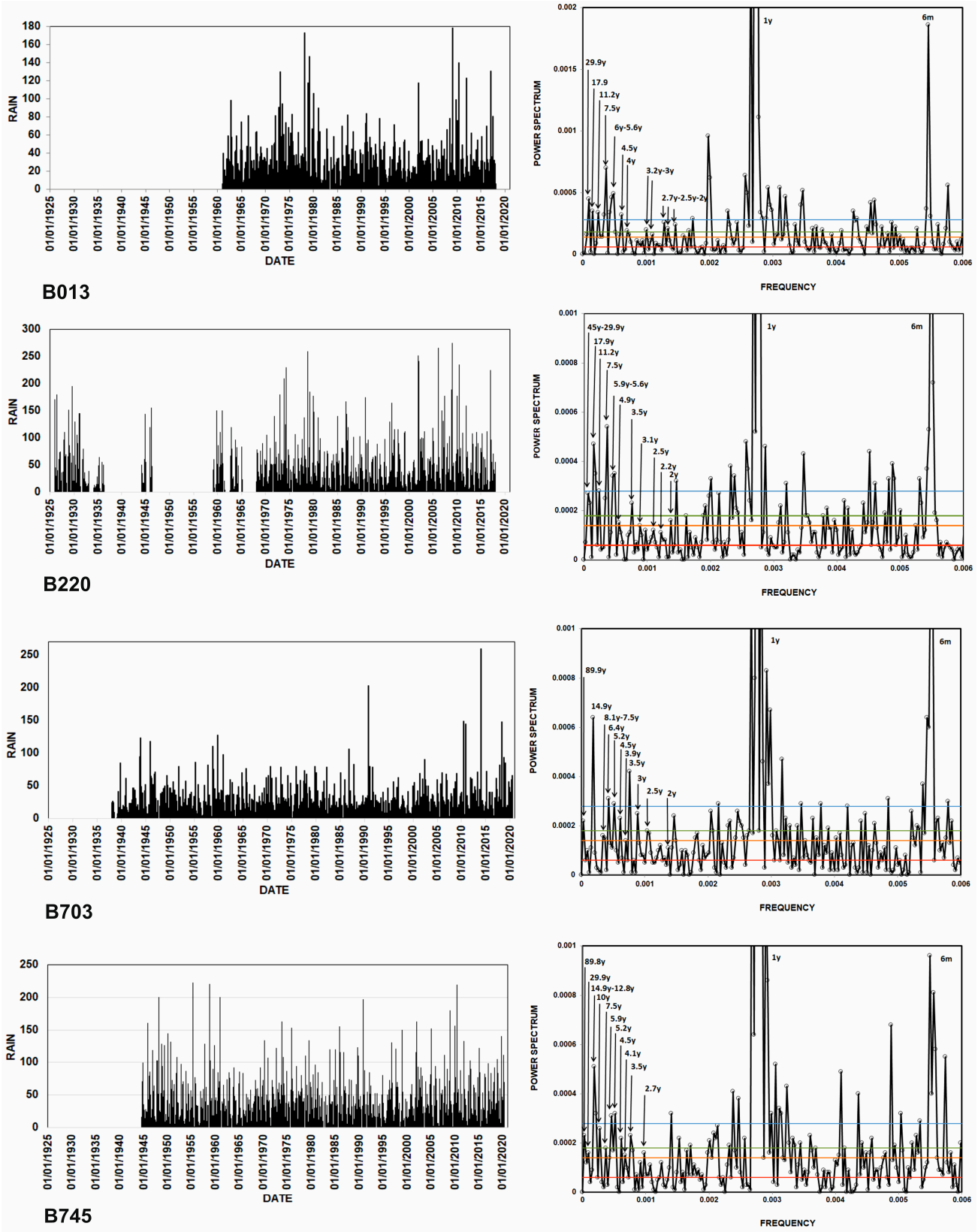


Figure 5. Rainfall records and results of the spectral analysis. Blue line > 99% statistical confidence. Green line > 95% spectral confidence. Orange line > 90% statistical confidence. Red line < 90% statistical confidence.

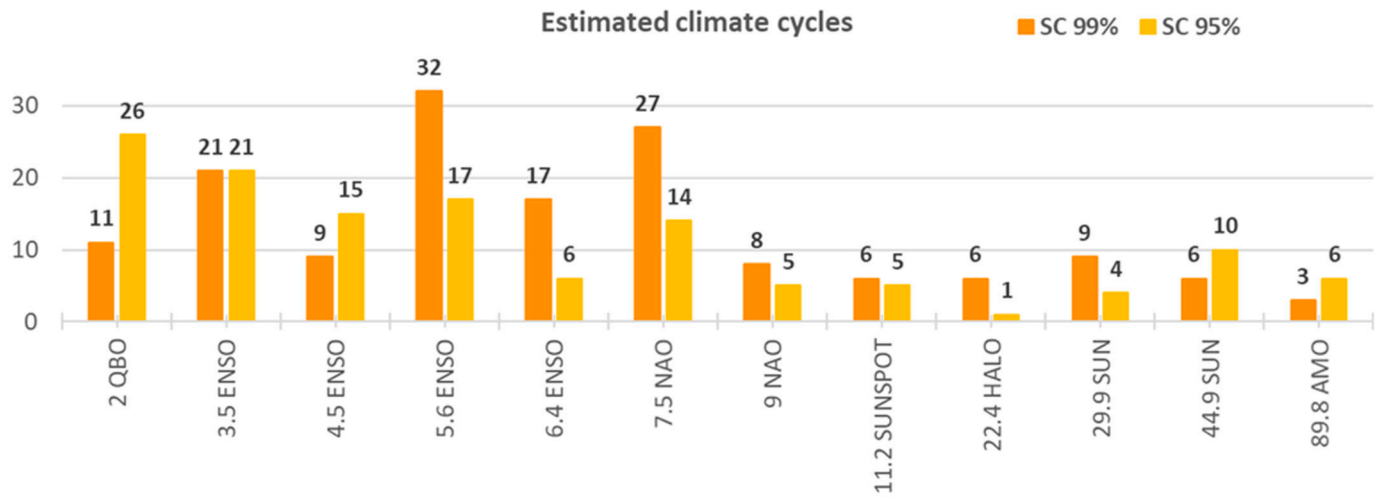


Figure 6. Main estimated climate cycles and spectral confidence values.

The mapped cycles affecting the whole island are ENSO (5.6 y), the NAO (7.5 y), ENSO (3.5 y), and QBO (Figure 7a–d). The 6.4 y (ENSO/the NAO) (Figure 7e), 11.2 y (Sunspot) (Figure 7f), and 22.4 y (HALO) (Figure 7g) cycles, which, in some meteorological series, have not been identified with sufficient clarity, do not affect the whole island. According to the results obtained, the ENSO cycle (5.6 y) influences the whole island, although the highest values are concentrated in sectors of the south coast, in the municipalities of Campos, Santanyí, and Ses Salines and in municipalities located in the Tramuntana range, such as Escorça, Campanet, Bunyola, Santa Maria del Camí, Valldemossa, and Andratx. The NAO cycle (7.5 y) presents the highest values distributed in different parts of the island, especially in relation to the Tramuntana range (municipalities of Palma, Marratxí, Bunyola, and Esporles), southern coastal areas (Ses Salines, Campos, and Santanyí), and the eastern coast (San Serverva and Sant Llorenç). The ENSO cycle (3.5 y) particularly affects a strip of municipalities located to the south of the Tramuntana range, between the municipalities of Sencelles and Inca and up to Alcúdia. However, it should also be taken into account that the lowest value of this cycle is close to 2, i.e., a probability greater than 90%. The QBO cycle shows the highest values of spectral confidence on the west coast, in the municipalities of Fornalutx, Escorça, Sóller, Bunyola, Campanet, and Pollença. The highest probabilities of the influence of the 6.4 y cycle (ENSO/the NAO) are to be found in some municipalities on the south and east coast of the island, mainly Llucmajor, Manacor, Felanitx, and Santanyí. The sunspot cycle is more likely to affect sectors linked to the west and north coast of the island, especially the municipalities of Banyalbufar, Puigpunyent, Esporles, Valldemossa, Escorça, Pollensa, and Artá. Finally, the HALO cycle is most significant in Santa María del Camí, Marratxi, Palma, Escorça, Pollença, Buyonla, Alaro, Sóller, and Consell.

Overall, the NW of the island is where the highest spectral confidence values are concentrated for all the above mentioned cycles and some sectors of the east coast. The central area of the Serra de Tramuntana, Bunyola–Fornalutx–Escorça–Sóller, stands out, with high spectral confidence values for practically all the cycles.

Regarding the location of the five instances of heaviest RF (Table 2) on the spectral confidence maps of the climate cycles, all of them include one or more of the detachments in the areas of greatest significance, with the NAO (7.5 y), QBO, and HALO (22.4 y)—as well as, to a lesser extent, sunspot—being the best fit.

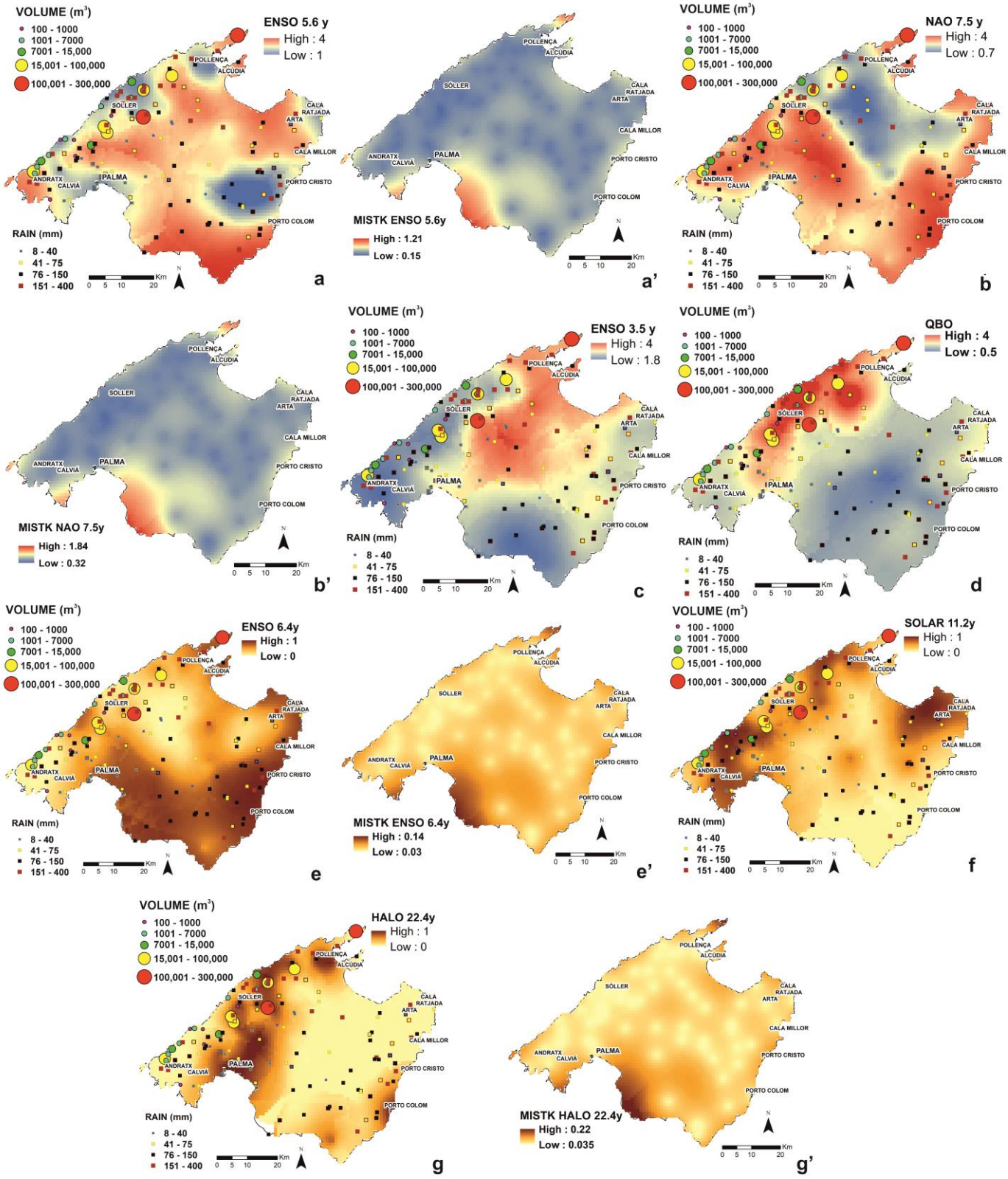


Figure 7. Spatial estimation of the spectral confidence of the climatic cycles with the greatest influence on the island of Mallorca using geostatistical methods. (**a**–**d**) have been estimated by Ordinary Kriging and (**e**–**g**) have been estimated by Indicator Kriging. (**a′**,**b′**,**e′**,**g′**) show the estimation error. The rockfalls are located and classified by volume. Rainfall: data from weather stations and associated with flash flood events recorded between 1932 and 2010 are presented in Table 3.

4.3. Spatial Analysis of Dry, Wet, and Normal Years

To complement the spectral analysis, the daily rainfall data have been transformed into annual data to study the spatio-temporal behavior of rainfall in an average-, wet-, and dry-type year. A selection has also been made of a series of years whose stations present values that are very similar or equal to the estimated-type years. The objective of this analysis was to determine the spatial behavior of rainfall in different periods, especially during rainy periods, when it can cause flooding or landslides.

Figure 8 shows the variogram models fitted to the calculated model years and the selected years. Two experimental variograms have been added: for a wet-type year (red) and a dry-type year (blue). All the estimated experimental variograms exhibited a very similar graphical distribution. In all cases, the theoretical variogram fitted was a spherical model, with a similar nugget effect and similar range. This behavior of the variograms is known as the proportional effect and indicates that the variable behaves in space and time in the same way, i.e., it presents the same spatial variability model. The proportional effect means that the variograms exhibit proportionality when the values of the semivariogram (γ(h)) at the origin are similar, the model is the same, and the range is very similar. The difference lies in the value of the sill (variance), which varies according to a multiplier factor. Overall, the value of the nugget effect is low in percentage terms, indicating that the variable is very continuous at the origin despite the fact that in some areas of the island the number of rainfall stations is lower. The only difference is the value of the sill, whose value coincides with the variance in the data. This behavior is potentially of great interest for developing predictive rainfall models for different climate change scenarios, whether or not the spatial behavior of the rainfall variable defined by the variograms changes.

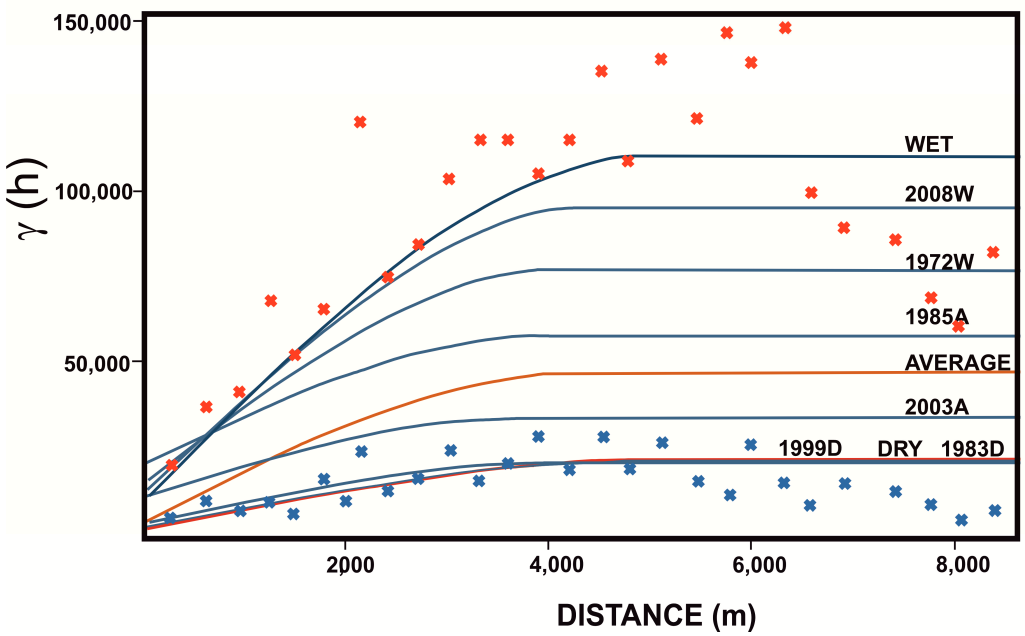


Figure 8. Theoretical variograms fitted for each of the dates selected for the spatial estimation of precipitation. Red cross: experimental variogram of wet-type year. Blue cross: experimental variogram of dry-type year.

As an example of the estimation of the type years and selected years, Figure 9 shows the spatial estimation of the wet-type year and the year 2008, the wettest of the years studied. Estimates were made from the fitted variogram models (Figure 8).

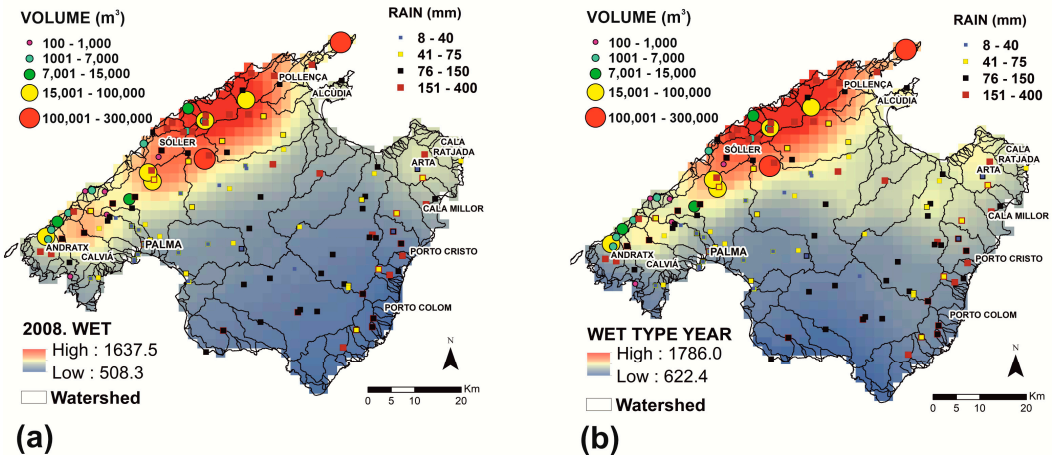


Figure 9. Estimated rainfall in mm in the year 2008 (**a**) and wet-type year (**b**), with similar values to those of the wet-type year. The landslides are located and classified by volume.

From the spatial point of view, the estimation of rainfall according to the fitted variogram models shows a very similar distribution in space and is always strongly influenced by the Tramuntana range, where the maximum values can be seen in all studied cases, especially in the areas oriented to the north and northwest and towards the coast as a whole. On the other hand, the minimum values are located towards the south of the island.

One should also note the great coincidence between the sector where the maximum rainfall is concentrated and the area of maximum probability of the main climatic cycles affecting the island. In this sense, if we look at Figure 9 (maximum rainfall) and compare it with Figure 7a,b,d,f,g, a significant part of the maximum probability of occurrence of these cycles coincides with the area of maximum rainfall recorded on the island. The rest of the cycles show a lower percentage of coincidence.

The superimposition of the landslides on Figure 9a,b shows a very good spatial correlation between the location of these landslides and the areas of highest rainfall in the typical wet year and in 2008. It coincides with the NE sector of the Serra de Tramuntana, where the relief is more pronounced. Specifically, the Son Cocó and Gorg Blau landslides (Figure 2) took place in December 2008, the latter being located exactly in the core of the wettest sector.

4.4. Relationship between Climate Cycles and Geohazards

The RF inventory is limited to the Serra de Tramuntana, while the flash flood data encompass the entire island, resulting in stronger validation of the results. Thus, to understand the relationship between climate indices and flash floods and landslides, we have analyzed the last annual indices of QBO, ENSO, the NAO and sunspots. The results of this comparison, as shown in Table 3, indicate that the QBO, NAO, ENSO, and sunspot cycles have the greatest influence on flash floods and landslides, although with some variations. This finding is consistent with the spatial estimation of these cycles.

The most significant events associated with flash floods are observed in the Serra de Tramuntana region, where they are primarily linked to the QBO and NAO cycles, with sunspots having a secondary influence. The second area most affected by flash floods is the southeast coast of the island, where the average precipitation is less than half that of the Serra de Tramuntana. In this case, the ENSO (6.4 y) and NAO cycles have the most significant impact.

4.5. Impact on the Urban Areas

Figure 10 illustrates the superposition, over urban areas, of the most influential climatic cycles on the island (QBO; 3.5 y, 7.5 y and 5.6 y cycles). The limits depicted for the climatic cycles represent the third quartile of the estimated data range, although this boundary

may vary depending on whether the cutoff criterion is more or less restrictive. While various parts of the island are affected by these cycles, the central and eastern regions, where these climatic patterns intersect, exhibit a pronounced impact. It is worth noting that apart from Palma, situated in the southwest of Mallorca, the concentration of urban areas predominantly lies in the central and eastern regions of the island.

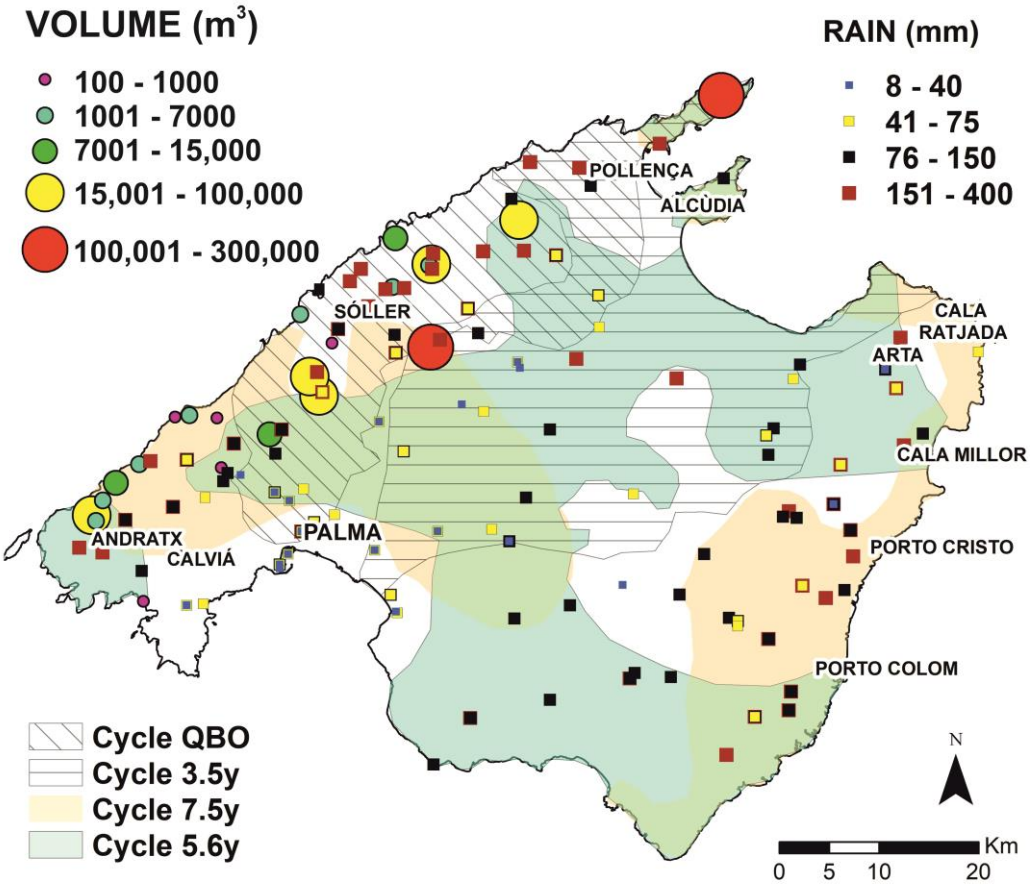


Figure 10. Superposition over urban areas of the most influential climatic cycles on the island (QBO; 3.5 y, 7.5 y, and 5.6 y cycles), where boundaries are defined according to the value of the third quartile of the estimated data range. The landslides are located (classified by volume), as well as extreme rainfall events recorded during the spanning period 2015–2022.

Concerning the rainfall recorded within 48 h, leading to flooding, values exceeding 151 mm/48 h are primarily concentrated in the Tramuntana area, characterized by lesser urban development. Nonetheless, highly urbanized towns such as Sóller, Andratx, Pollença, and Calviá are situated within this zone, posing a significant risk of flash floods due to sporadic torrential activity. The Serra de Tramuntana region also experiences the strongest influence from the QBO cycle.

The second area with notable concentrations of heavy rainfall in 48 h is the eastern part of the island, witnessing numerous instances of rainfall exceeding 151 mm/48 h, as well as ranging between 76 mm/48 h and 150 mm/48 h. This region harbors several tourist resorts along the coast, including Porto Cristo, Porto Colom, Cala Millor, and Cala Ratjada.

In assessing the impact on urban areas in Mallorca, heavy rainfall incidents from the period 2015–2022 have been considered. Figure 9 depicts a higher occurrence of such events in the northern half of the island, particularly in densely populated towns like Pollença, Alcudia, and Artà.

The city of Palma (the capital of Mallorca) and the municipality of Calvià also emerge prominently, featuring numerous documented instances of heavy rainfall. The maps in

Figure 9 indicate that the majority of the most densely populated and urbanized areas in Mallorca are situated in regions most vulnerable to intense rainfall and its consequences.

Table 4 shows in percentage terms the degree of influence of the climatic cycles represented in Figure 10. Relatively, QBO is the cycle that most influences both floods and landslides because it affects 20% of the island. However, the NAO is the cycle that has mobilized the most water and rock during the study period.

Table 4. SUP: Percentage of the climatic cycle's influence over the entire island of Mallorca. FF: Percentage of climatic stations related to each cycle (Table 3). RAIN: Total volume of water collected in each cycle at the climatic stations shown in Table 3. LS: Percentage of landslides occurring in each cycle. VR: Volume of rock mobilized in each cycle according to Table 2.

CYCLE	SUP (%)	FF (%)	RAIN (Litres)	LS (%)	VR (m^3)
QBO	20%	32%	16,398	50%	341,200
3.5 y	35%	18%	7240	9%	500,000
7.5 y	39%	47%	22,940	54%	569,300
5.6 y	56%	43%	17,350	36%	297,200

5. Discussion and Conclusions

This study is framed in probabilistic terms. In this context, sectors have been identified where there is a high probability of them being affected by certain climatic cycles and where these cycles are likely to influence the geological hazards analyzed.

The spectral analysis has made it possible to identify the climatic cycles that determine the behavior of rainfall on the island of Mallorca. The lower-frequency cycles (>30 y) offer doubts regarding the real influence on all the stations, as the historical records are not sufficiently extensive. If all stations had, at least, 100 years of records, the analysis of these would allow us to ascertain with certainty the degree of influence of these cycles throughout the island.

The cycles with the greatest influence on the pluviometry of the study area, from the point of view of spectral confidence, are 5.6 y (the ENSO), 7.5 y (the NAO), 3.5 y (the ENSO), the QBO, and, with less weight, 6.4 y (ENSO or NAO) and 4.5 y (the ENSO).

The reclassification of the results of the spectral analysis has made it possible to map the influence of climatic cycles in Mallorca using geostatistical methods. The variogram models adjusted to the spectral confidence variables reflect very continuous behavior in space, which made it possible to generate cartographies that clearly show the different climatic influences in the working area. In this context, continuity means that the fitted variograms exhibit a low nugget effect percentage, indicating that the unstructured part of the estimation has little influence. The estimation errors obtained underscore the imperative for augmenting the number of rain gauge stations to enhance rainfall estimations, particularly in regions like Mallorca characterized by sporadic, intense precipitation events. The spatial variability in rainfall represented by the variograms and the presence of a proportional effect in the variograms indicate that the spatial behavior of the variable is independent on the amount of rainfall. The sectors where the maximum rainfall is concentrated show a variable degree of coincidence, with the maximum values of spectral confidence of the climatic cycles that most influence the island. In this sense, the highest coincidence, in decreasing order, is QBO, the NAO 7.5 y, sunspots, HALO, ENSO 5.6 y, ENSO 3.5 y, and ENSO/the NAO 6.4 y. The prominent influence of QBO suggests its integration, to varying extents, with lower-frequency cycles, as corroborated by multiple authors.

The Serra de Tramuntana, to the NW of the island, is not only the rainiest region of the island but also the area where the highest values of spectral confidence for the set of climatic cycles are concentrated. In this region, 423 landslides have been inventoried in the last 30 years. The five landslides with the highest magnitude in the series are located in the areas with the highest spectral confidence.

The intense precipitation that triggers landslides in the Serra de Tramuntana is linked to the ENSO and NAO cycles, together with sunspots and HALO. An important novelty in this work is the influence exerted by QBO, whose spatial estimation of spectral confidence shows the highest values in the areas where the five largest landslides are located, as well as data on flash-flood-related rainfall events also having been analyzed. In the Sóller area, three significant factors converge concerning landslides: pronounced gradients, the intense precipitation primarily correlated, and susceptible lithologies.

The validation of the influence of climatic cycles on geohazards is more robust with the use of data from physical phenomena which encompass the entire island, versus data limited to RF in the Serra de Tramuntana. The recorded events of flash floods and RF exhibit a strong correlation with the climate indices of Quasi-Biennial Oscillation (QBO), El Niño–Southern Oscillation (ENSO), North Atlantic Oscillation (NAO), and sunspot activity. This correlation is particularly pronounced with QBO, as this cycle, which has a higher frequency than the others, is observed as part of the others in the form of increases and decreases during periods of higher ENSO, NAO, and sunspot values. This observation explains the significant similarity between the spatial distribution of annual rainfall and the influence of QBO. However, the impact of flash floods is also significant in the southeast, despite the lower levels of rainfall. The most dangerous episodes are related to ENSO (6.4 y) and the NAO, with the influence of QBO being negligible. Thus, topography plays a crucial role in determining the differences in precipitation and the most influential cycles that mark the occurrence of geological hazards.

The central and eastern areas of the island are where a greater overlap of climatic cycles, with significant influence on the occurrence of extreme rainy events, is identified. These regions coincide with the majority of the most urbanized areas in Mallorca, making them particularly vulnerable to intense rainfall and its consequences.

The city of Palma (the capital of Mallorca) and the municipality of Calvià also emerge prominently, featuring numerous documented instances of heavy rainfall. Both areas are the most densely populated on the island.

The methodology presented in this work is applicable to any case study that has sufficient meteorological stations and historical rainfall records and can be related to other geological hazards linked to water, such as floods or landslides. In this sense, this type of analysis offers a calibrated and validated instrument to the institutions responsible for emergency management, which can be extremely useful for decision-making in the face of these types of geological hazards.

Author Contributions: J.A.L.-E. (IGME-CSIC) led and designed the study, wrote the paper, was involved in data curation and analysis, and interpreted the results; R.M.M. (IGME-CSIC) collaborated in the writing and reviewing of the paper, analyzing the data, and interpretation; R.S. (IGME-CSIC) collaborated in writing, the preparation of some figures, and analyzing and interpreting the data and formatted the text; C.R.-C. (UNIMIB) and M.M.-C. (IGME-CSIC) were involved in reviewing and helped in collecting data. All authors have read and agreed to the published version of the manuscript.

Funding: This work was developed in the framework of the RISKCOAST project (Ref: SOE3/P4/E0868), funded by the Interreg SUDOE programme (third call for proposals). Many thanks to AEMET (the Spanish Meteorological Agency) for the rainfall data, as well as to the Road Maintenance Service of Mallorca and the Emergency Services of the Balearic Islands, for providing information on many landslide events.

Institutional Review Board Statement: Not applicable.

Informed Consent Statement: Not applicable.

Data Availability Statement: The data presented in this paper are available on request from the corresponding author. The data are not publicly available due to privacy.

Acknowledgments: We would like to thank Jordi Giménez (Water Service of the Balearic Government), as well as Francisca González and Margalida Obrador (Emergency Services of the Balearic Government), for their invaluable help in collecting the data for this work.

Conflicts of Interest: The authors declare no conflicts of interest.

References

1. Mateos, R.M.; Sarro, R.; Díez-Herrero, A.; Reyes-Carmona, C.; López-Vinielles, J.; Ezquerro, P.; Martínez-Corbella, M.; Bru, G.; Luque, J.A.; Barra, A.; et al. Assessment of the Socio-Economic Impacts of Extreme Weather Events on the Coast of Southwest Europe during the Period 2009–2020. *Appl. Sci.* **2023**, *13*, 2640. [CrossRef]
2. Grimalt-Gelabert, M.; Rosselló-Geli, J.; Bauzà-Llinàs, J. Flood Related Mortality in a Touristic Island: Mallorca (Balearic Islands) 1960–2018. *J. Flood Risk Manag.* **2020**, *13*, e12644. [CrossRef]
3. Lorenzo-Lacruz, J.; Amengual, A.; Garcia, C.; Morán-Tejeda, E.; Homar, V.; Maimó-Far, A.; Hermoso, A.; Ramis, C.; Romero, R. Hydro-Meteorological Reconstruction and Geomorphological Impact Assessment of the October 2018 Catastrophic Flash Flood at Sant Llorenç, Mallorca (Spain). *Nat. Hazards Earth Syst. Sci.* **2019**, *19*, 2597–2617. [CrossRef]
4. Richard Eiser, J.; Bostrom, A.; Burton, I.; Johnston, D.M.; McClure, J.; Paton, D.; van der Pligt, J.; White, M.P. Risk Interpretation and Action: A Conceptual Framework for Responses to Natural Hazards. *Int. J. Disaster Risk Reduct.* **2012**, *1*, 5–16. [CrossRef]
5. Luque-Espinar, J.A.; Mateos, R.M.; García-Moreno, I.; Pardo-Igúzquiza, E.; Herrera, G. Spectral Analysis of Climate Cycles to Predict Rainfall Induced Landslides in the Western Mediterranean (Majorca, Spain). *Nat. Hazards* **2017**, *89*, 985–1007. [CrossRef]
6. Xoplaki, E.; Trigo, R.M.; García-Herrera, R.; Barriopedro, D.; D'Andrea, F.; Fischer, E.M.; Gimeno, L.; Gouveia, C.; Hernández, E.; Kuglitsch, F.G.; et al. Large-Scale Atmospheric Circulation Driving Extreme Climate Events in the Mediterranean and Its Related Impacts. In *The Climate of the Mediterranean Region*; Lionello, P., Ed.; Elsevier: Oxford, UK, 2012; pp. 347–417. ISBN 978-0-12-416042-2.
7. Muñoz-Díaz, D.; Rodrigo, F.S. Influence of the El Niño-Southern Oscillation on the Probability of Dry and Wet Seasons in Spain. *Clim. Res.* **2005**, *30*, 1–12. [CrossRef]
8. Rodó, X.; Baert, E.; Comín, F.A. Variations in Seasonal Rainfall in Southern Europe during the Present Century: Relationships with the North Atlantic Oscillation and the El Niño-Southern Oscillation. *Clim. Dyn.* **1997**, *13*, 275–284. [CrossRef]
9. Tramblay, Y.; El Adlouni, S.; Servat, E. Trends and Variability in Extreme Precipitation Indices over Maghreb Countries. *Nat. Hazards Earth Syst. Sci.* **2013**, *13*, 3235–3248. [CrossRef]
10. Labitzke, K.; van Loon, H.; Shine, K.; Pecker, J.-C.; Runcorn, S.K. Associations between the 11-Year Solar Cycle, the Quasi-Biennial Oscillation and the Atmosphere: A Summary of Recent Work. Philosophical Transactions of the Royal Society of London. *Ser. A Math. Phys. Sci.* **1990**, *330*, 577–589. [CrossRef]
11. Stuiver, M.; Braziunas, T. Atmospheric 14C and Century-Scale Solar Oscillations. *Nature* **1989**, *338*, 405–408. [CrossRef]
12. Fleming, S.W.; Quilty, E.J. Aquifer Responses to El Niño–Southern Oscillation, Southwest British Columbia. *Groundwater* **2006**, *44*, 595–599. [CrossRef] [PubMed]
13. Hurrell, J.W. Decadal Trends in the North Atlantic Oscillation: Regional Temperatures and Precipitation. *Science* **1995**, *269*, 676–679. [CrossRef] [PubMed]
14. Pozo-Vázquez, D.; Esteban-Parra, M.J.; Rodrigo, F.S.; Castro-Díez, Y. An Analysis of the Variability of the North Atlantic Oscillation in the Time and the Frequency Domains. *Int. J. Climatol.* **2000**, *20*, 1675–1692. [CrossRef]
15. Hoyt, D.V.; Schatten, K.H. *The Role of the Sun in Climate Change*; Oxford University Press: Oxford, UK, 1997; ISBN 978-0-19-535748-6.
16. Currie, R.G.; Wyatt, T.; O'Brien, D.P. Deterministic Signals in European Fish Catches, Wine Harvests, and Sea-Level, and Further Experiments. *Int. J. Climatol.* **1993**, *13*, 665–687. [CrossRef]
17. Pardo-Igúzquiza, E.; Rodríguez-Tovar, F.J. Spectral and Cross-Spectral Analysis of Uneven Time Series with the Smoothed Lomb–Scargle Periodogram and Monte Carlo Evaluation of Statistical Significance. *Comput. Geosci.* **2012**, *49*, 207–216. [CrossRef]
18. Williams, G.E. Sunspot Periods in the Late Precambrian Glacial Climate and Solar–Planetary Relations. *Nature* **1981**, *291*, 624–628. [CrossRef]
19. Hoeppe, P. Trends in Weather Related Disasters–Consequences for Insurers and Society. *Weather Clim. Extrem.* **2016**, *11*, 70–79. [CrossRef]
20. Wills, R.C.J.; Armour, K.C.; Battisti, D.S.; Hartmann, D.L. Ocean–Atmosphere Dynamical Coupling Fundamental to the Atlantic Multidecadal Oscillation. *J. Clim.* **2019**, *32*, 251–272. [CrossRef]
21. Eleftheratos, K.; Zerefos, C.S.; Balis, D.S.; Koukouli, M.-E.; Kapsomenakis, J.; Loyola, D.G.; Valks, P.; Coldewey-Egbers, M.; Lerot, C.; Frith, S.M.; et al. The Use of QBO, ENSO, and NAO Perturbations in the Evaluation of GOME-2 MetOp A Total Ozone Measurements. *Atmos. Meas. Tech.* **2019**, *12*, 987–1011. [CrossRef]
22. Neyestani, A.; Karami, K.; Gholami, S. Exploring the Possible Linkage between the Precipitation and Temperature over Iran and Their Association with the Large-Scale Circulations: Cumulative Spectral Power and Wavelet Coherence Approaches. *Atmos. Res.* **2022**, *274*, 106187. [CrossRef]
23. Zeng, Y.; Zhang, J.; Li, Y.; Liu, S.; Chen, H. Wavelet Analysis of Ozone Driving Factors Based on ~20 Years of Ozonesonde Measurements in Beijing. *Atmosphere* **2023**, *14*, 1733. [CrossRef]
24. Jury, M.R.; Mc Queen, C.; Levey, K. SOI and QBO Signals in the African Region. *Theor Appl Clim.* **1994**, *50*, 103–115. [CrossRef]

25. Sánchez-Morales, J.; Pardo-Igúzquiza, E.; Rodríguez-Tovar, F.J. Spatial Distribution of Climatic Cycles in Andalusia (Southern Spain). In Proceedings of the Theory and Applications of Time Series Analysis; Valenzuela, O., Rojas, F., Pomares, H., Rojas, I., Eds.; Springer International Publishing: Cham, Germany, 2019; pp. 243–255.
26. Rodrigo, F.S.; Esteban-Parra, M.J.; Pozo-Vázquez, D.; Castro-Díez, Y. Rainfall Variability in Southern Spain on Decadal to Centennial Time Scales. *Int. J. Climatol.* **2000**, *20*, 721–732. [CrossRef]
27. Jenkins, G.M.; Watts, D.G. *Spectral Analysis and Its Applications*; Holden-Day Series in Time Series Analysis; Holden-Day: San Francisco, CA, USA, 1968; ISBN 978-0-8162-4464-5.
28. Karagiannidis, A.F.; Bloutsos, A.A.; Maheras, P.; Sachsamanoglou, C. Some Statistical Characteristics of Precipitation in Europe. *Theor. Appl. Climatol.* **2008**, *91*, 193–204. [CrossRef]
29. Knippertz, P. Tropical–Extratropical Interactions Causing Precipitation in Northwest Africa: Statistical Analysis and Seasonal Variations. *Mon. Weather Rev.* **2003**, *131*, 3069–3076. [CrossRef]
30. Corominas, J. El clima y sus consecuencias sobre la actividad de los movimientos de ladera en España. *Cuaternario y Geomorfol.* **2006**, *20*, 89–113.
31. Capparelli, G.; Versace, P. FLaIR and SUSHI: Two Mathematical Models for Early Warning of Landslides Induced by Rainfall. *Landslides* **2011**, *8*, 67–79. [CrossRef]
32. Guzzetti, F.; Peruccacci, S.; Rossi, M.; Stark, C.P. The Rainfall Intensity–Duration Control of Shallow Landslides and Debris Flows: An Update. *Landslides* **2008**, *5*, 3–17. [CrossRef]
33. Huang, J.; Ju, N.P.; Liao, Y.J.; Liu, D.D. Determination of Rainfall Thresholds for Shallow Landslides by a Probabilistic and Empirical Method. *Nat. Hazards Earth Syst. Sci.* **2015**, *15*, 2715–2723. [CrossRef]
34. Mathew, J.; Babu, D.G.; Kundu, S.; Kumar, K.V.; Pant, C.C. Integrating Intensity–Duration-Based Rainfall Threshold and Antecedent Rainfall-Based Probability Estimate towards Generating Early Warning for Rainfall-Induced Landslides in Parts of the Garhwal Himalaya, India. *Landslides* **2014**, *11*, 575–588. [CrossRef]
35. Melillo, M.; Gariano, S.L.; Peruccacci, S.; Sarro, R.; Mateos, R.M.; Brunetti, M.T. Rainfall and Rockfalls in the Canary Islands: Assessing a Seasonal Link. *Nat. Hazards Earth Syst. Sci. Discuss.* **2020**, *2020*, 1–26. [CrossRef]
36. Piciullo, L.; Gariano, S.L.; Melillo, M.; Brunetti, M.T.; Peruccacci, S.; Guzzetti, F.; Calvello, M. Definition and Performance of a Threshold-Based Regional Early Warning Model for Rainfall-Induced Landslides. *Landslides* **2017**, *14*, 995–1008. [CrossRef]
37. Schuster, R.L.; Turner, A.K. *Landslides: Investigation and Mitigation*; National Academy Press: Washington, DC, USA, 1996; ISBN 978-0-309-06151-3.
38. Staley, D.M.; Kean, J.W.; Cannon, S.H.; Schmidt, K.M.; Laber, J.L. Objective Definition of Rainfall Intensity–Duration Thresholds for the Initiation of Post-Fire Debris Flows in Southern California. *Landslides* **2013**, *10*, 547–562. [CrossRef]
39. Terlien, M.T.J. The Determination of Statistical and Deterministic Hydrological Landslide-Triggering Thresholds. *Environ. Geol.* **1998**, *35*, 124–130. [CrossRef]
40. Wieczorek, G.F.; Guzzetti, F. A Review of Rainfall Thresholds Tor Triggering Landslides. In Proceedings of the Mediterranean Storms 1999—Proceedings EGS Plinius Conference, Maratea, Italy, 14–16 October 1999.
41. Palenzuela Baena, J.A.; Soto Luzuriaga, J.; Irigaray Fernández, C. Characteristics of Rainfall Events Triggering Landslides in Two Climatologically Different Areas: Southern Ecuador and Southern Spain. *Hydrology* **2020**, *7*, 45. [CrossRef]
42. Soto, J.; Palenzuela, J.A.; Galve, J.P.; Luque, J.A.; Azañón, J.M.; Tamay, J.; Irigaray, C. Estimation of Empirical Rainfall Thresholds for Landslide Triggering Using Partial Duration Series and Their Relation with Climatic Cycles. *Appl. South. Ecuador. Bull Eng Geol Env.* **2019**, *78*, 1971–1987. [CrossRef]
43. Nobre, G.G.; Jongman, B.; Aerts, J.; Ward, P.J. The Role of Climate Variability in Extreme Floods in Europe. *Environ. Res. Lett.* **2017**, *12*, 084012. [CrossRef]
44. Sun, Q.; Miao, C.; AghaKouchak, A.; Duan, Q. Century-scale Causal Relationships between Global Dry/Wet Conditions and the State of the Pacific and Atlantic Oceans. *Geophys. Res. Lett.* **2016**, *43*, 6528–6537. [CrossRef]
45. Steirou, E.; Gerlitz, L.; Apel, H.; Merz, B. Links between Large-Scale Circulation Patterns and Streamflow in Central Europe: A Review. *J. Hydrol.* **2017**, *549*, 484–500. [CrossRef]
46. Mateos, R.M.; García-Moreno, I.; Azañón, J.M. Freeze–Thaw Cycles and Rainfall as Triggering Factors of Mass Movements in a Warm Mediterranean Region: The Case of the Tramuntana Range (Majorca, Spain). *Landslides* **2012**, *9*, 417–432. [CrossRef]
47. Mateos, R.M.; Azañón, J.M.; Morales, R. Regional Prediction of Landslides in the Tramuntana Range (Majorca) Using Probability Analysis of Intense Rainfall. *Zeitschrift für Geomorphologie* **2007**, *51*, 287–306. [CrossRef]
48. Mateos, R.M. Los Movimientos de Ladera En La Serra de Tramuntana (Mallorca): Caracterización Geomecánica y Análisis de Peligrosidad. Ph.D. Thesis, Universidad Complutense de Madrid, Madrid, Spain, 2006.
49. Mateos, R.M.; García-Moreno, I.; Reichenbach, P.; Herrera, G.; Sarro, R.; Rius, J.; Aguiló, R.; Fiorucci, F. Calibration and Validation of Rockfall Modelling at Regional Scale: Application along a Roadway in Mallorca (Spain) and Organization of Its Management. *Landslides* **2016**, *13*, 751–763. [CrossRef]
50. Bras, R.L.; Rodríguez-Iturbe, I. *Random Functions and Hydrology*; Courier Corporation: North Chelmsford, MA, USA, 1993; ISBN 978-0-486-67626-5.
51. Yevjevich, V.M. *Stochastic Processes in Hydrology*, 1st ed.; WRP | Water Resources Publications, LLC: Littleton, CO, USA, 1972; ISBN 978-1-887201-77-3.

52. Blackman, R.B.; Tukey, J.W. The Measurement of Power Spectra from the Point of View of Communications Engineering—Part I. *Bell Syst. Tech. J.* **1958**, *37*, 185–282. [CrossRef]
53. Pardo-Igúzquiza, E.; Rodríguez-Tovar, F.J. POWGRAF2: A Program for Graphical Spectral Analysis in Cyclostratigraphy. *Comput. Geosci.* **2004**, *30*, 533–542. [CrossRef]
54. Lomb, N.R. Least-Squares Frequency Analysis of Unequally Spaced Data. *Astrophys Space Sci.* **1976**, *39*, 447–462. [CrossRef]
55. Scargle, J.D. Studies in Astronomical Time Series Analysis. II. Statistical Aspects of Spectral Analysis of Unevenly Spaced Data. *Astrophys. J.* **1982**, *263*, 835–853. [CrossRef]
56. Chiles, J.-P.; Delfiner, P. *Geostatistics: Modeling Spatial Uncertainty*, 2nd ed.; Wiley series in probability and statistics; Wiley: Hoboken, NJ, USA, 2012; ISBN 978-0470183151.
57. Deutsch, C.V.; Journel, A.G. *GSLIB: Geostatistical Software Library and User's Guide*; Oxford University Press: Oxford, UK, 1992; ISBN 978-0-19-507392-8.
58. Isaaks, E.H.; Srivastava, R.M. An Introduction to Applied Geostatistics. *Comput. Geosci.* **1991**, *17*, 471–473. [CrossRef]
59. Matheron, G. *Les Variables Regionalisees et leur Estimation: Une Application de la Theorie de Fonctions Aleatoires aux Sciences de la Nature*; Masson et Cie: Échandens, Switzerland, 1965.

Disclaimer/Publisher's Note: The statements, opinions and data contained in all publications are solely those of the individual author(s) and contributor(s) and not of MDPI and/or the editor(s). MDPI and/or the editor(s) disclaim responsibility for any injury to people or property resulting from any ideas, methods, instructions or products referred to in the content.